Published in final edited form as:
J Phys Chem C Nanomater Interfaces. 2009 July 1; 113(31): 13906–13917. doi:10.1021/jp902736z.

Ammonia Vapor Removal by $Cu_3(BTC)_2$ and Its Characterization by MAS NMR

Gregory W. Peterson*, **George W. Wagner**, **Alex Balboa**, **John Mahle**, **Tara Sewell**, and **Christopher J. Karwacki**

[†]Edgewood Chemical Biological Center, 5183 Blackhawk Rd., APG, MD 21010-5424

Abstract

Adsorption equilibria and NMR experiments were performed to study the adsorption and interactions of ammonia with metal-organic framework (MOF) HKUST-1, or $Cu_3(BTC)_2$ (BTC = 1,3,5-benzenetricarboxylate). Ammonia capacities determined from chemical breakthrough measurements show significantly higher uptake capacities than from adsorption alone, suggesting a stronger interaction involving a potential reaction with the $Cu_3(BTC)_2$ framework. Indeed, ^{1}H MAS NMR reveals that a major disruption of the relatively simple spectrum of $Cu_3(BTC)_2$ occurs to generate a composite spectrum consistent with $Cu(OH)_2$ and $(NH_4)_3BTC$ species under humid conditions—the anticipated products of a copper(II) carboxylate reacted with limited ammonia. These species are not detected under dry conditions; however, reaction stoichiometry combined with XRD results suggests the partial formation of an indeterminate diammine copper (II) complex with some residual $Cu_3(BTC)_2$ structure retained. Cu(II)-induced paramagnetic shifts exhibited by various species in ^{1}H and ^{13}C MAS NMR spectra are consistent with model compounds and previous literature. Although results show extensive ammonia capacity of $Cu_3(BTC)_2$, much of the capacity is due to reaction with the structure itself, causing a permanent loss in porosity and structural integrity.

Keywords

HKUST-1; Metal-organic frameworks; MOFs; porous coordination polymers; PCP; ammonia; air purification; filtration; paramagnetic NMR

Introduction

Highly porous structures possessing functionalized active sites are essential for retention of light vapors. Permanent adsorption of ammonia presents a unique challenge due to its high vapor pressure and reversibility as a weakly bound ligand. Although a number of adsorbent materials, such as activated carbons impregnated with copper chloride, have been shown to be effective during the initial uptake of ammonia, the adsorption affinities are sufficiently low such that ammonia desorption results from ambient temperature purge.[1–2] Because the commercially available adsorbents such as activated carbons and zeolites exhibit ammonia off-gassing even at low (10^{-5}) relative pressures or are ineffectual in the presence of humidity, more active sorbents are sought to reduce the volume of filtration systems. Of particular note are metal-organic frameworks (MOFs), or porous-coordination polymers (PCPs).

gregory.w.peterson@us.army.mil, phone : (410) 436-9794, fax : (410) 436-5513.

Supporting Information Available

Raw nitrogen isotherm data for fresh and ammonia-exhausted samples, ^{1}H and ^{13}C MAS NMR spectra for solvent extracted $Cu_3(BTC)_2$ and $(NH_4)_3BTC$, and XRD patterns of fresh and exposed $Cu_3(BTC)_2$ compared to Mercury simulations. This material is available free of charge via the Internet at http://pubs.acs.org.

MOFs represent a relatively new class of porous materials that can be tailored to modify surface area, pore size, functionality and topology through reticular chemistry, [3–6] a methodology advanced by Yaghi and coworkers. Reticular chemistry permits the synthesis of predetermined structures by utilizing a variety of inorganic and organic building blocks, thus allowing the development of high capacity materials customized for specific removal chemistries. Although the majority of work on MOFs to date has focused on gas storage applications, [7–10] this class of materials shows promise for a broad range of air purification applications. Reticular chemistry permits the synthesis of predetermined structures by utilizing a variety of inorganic and organic building blocks, thus allowing the development of high capacity materials customized for specific removal chemistries.

Although MOFs have been studied for over a decade, very limited data exist on dynamic removal of toxic gases in air purification applications.[11–13] Yaghi and coworkers [11] studied dynamic breakthrough of six MOFs against several toxic chemicals and found that pore structure and functionality played important roles in toxic gas removal. Lercher and coworkers [12–13] similarly studied the dynamic removal of SO_x by Cu-BTC analogs, and reported the oxidation of SO_x by impregnated Cu-BTC. Chui and coworkers[14] evaluated HKUST-1, or $Cu_3(BTC)_2$, for ammonia removal from contaminated air streams. $Cu_3(BTC)_2$ is formed by paddlewheel secondary building units (SBUs) containing Cu^{2+} dimers coordinatively linked to carboxylic oxygen atoms from organic benzene-1,3,5-tricarboxylate (BTC) ligands.[14–15] Previous studies have shown that, once formed, the copper atoms in $Cu_3(BTC)_2$ are unsaturated [14–15] and may therefore be available for chemisorption with ammonia, which is known to form coordination complexes with alkali and transition metals[1,17–18].

The reaction of ammonia with the individual building blocks of $Cu_3(BTC)_2$, i.e. Cu(II) ion and BTC, is well-known. In aqueous solution, Cu(II) ion, in the presence of limited ammonia, is initially converted to $Cu(OH)_2$; however, copious amounts of ammonia eventually yield $[Cu(NH_3)_4]^{2+}$ [22]. Carboxylic acids initially form the ammonium salt (Scheme 1) which, with sufficient heating, can be pyrolized to their corresponding amides [23]:

It is further noteworthy, in particular, that copper salts of aromatic acids (i.e., $Cu_3(BTC)_2$) are known to react with ammonia (with heating) to generate aromatic amines, [23] a reaction involving scission of the copper-carboxylate ionic bond.

Other studies conducted on gas sorption behavior of $Cu_3(BTC)_2$ as well as other open-metal site MOFs concluded that the unsaturated metal sites may contribute significantly to gas uptake [19–21]. Furthermore, the relatively weak acidic coordination bonds of the structure may provide additional reactive centers for ammonia removal. In this work we present a detailed study of the ammonia removal properties of $Cu_3(BTC)_2$ through breakthrough analysis, nitrogen isotherm data, PXRD, and MAS NMR.

Experimental

Materials

$Cu(acetate)_2(H_2O)$, Cu(*l*-tartrate)$_3(H_2O)_3$, $Cu(CO_3)Cu(OH)_2$, 1,3,5-benzenetricarboxylic acid, NH_4HCO_3, and *N*,*N*–dimethylformamide were obtained from Aldrich Chemical Co. and used without further purification.

$Cu_3(BTC)_2$ Synthesis

$Cu_3(BTC)_2$ was synthesized by Yaghi's group at UCLA[24]. Briefly, $Cu_3(BTC)_2$ was synthesized by stirring benzene-1,3,5-tricarboxylic acid and copper nitrate in a solvent consisting of *N*,*N*-dimethylformamide, ethanol, and deionized water. The reaction was allowed to proceed for approximately 24 hours at a temperature of 85°C, and subsequently immersed

in dichloromethane for 3 days. The crystals were activated under high vacuum at a temperature of 170°C.

Nitrogen Adsorption Equilibria

Nitrogen adsorption equilibria on clean and ammonia exposed $Cu_3(BTC)_2$ were measured on a Quantachrome Autosorb-1. Each sample of $Cu_3(BTC)_2$ was exposed to a relative pressures ranging from 10^{-5} to a maximum pressure of 1 atm. Adsorbed volumes were initially reported at STP and subsequently converted to equivalent liquid volumes at the boiling point of nitrogen. Pretreatment conditions for the unexposed and ammonia-exposed $Cu_3(BTC)_2$ were 150°C for 16 hrs under vacuum (approximately 1×10^{-9} atm).

Ammonia Breakthrough

A micro-scale breakthrough apparatus was developed to assess the adsorption and reaction behavior of adsorbent samples for air purification applications. The system was designed to operate at near ambient temperature over a range of humidities. A schematic of the test apparatus is presented in Figure 1. The test conditions are summarized in Table 1. Briefly, the system utilizes a small adsorbent sample size (approximately 5–10 mg) packed into a nominal 4 mm ID fritted glass tube. The chemical is delivered as a dilute gas stream using a gas sampling canister which has been purged with dry air and sealed. A measured volume of ammonia is injected into the canister through a septum using a gas tight syringe which is subsequently pressurized to 1 atmg. The contents were delivered by a calibrated mass flow controller, and verified with a bubble meter. The dry chemical stream was mixed with either a dry or humid air dilution stream to achieve a concentration of 1,000 mg/m^3 at the either dry (−40°C Dew point) or humid (80% relative humidity), and challenged to $Cu_3(BTC)_2$ samples at a flow rate of 20 sccm (referenced to 20°C). The effluent stream was continuously monitored for ammonia and water breakthrough to saturation with an FTIR (Nicolet 380, with DTGS detector).

A $Cu_3(BTC)_2$ sample was loaded into the sample tube and dried at 100°C in a nitrogen stream. The sample tube was then conditioned under dry or humid conditions. The ammonia challenge was then conducted until saturation and followed by then purged with a clean stream. Following the purge step, the once exposed samples were removed and dried at 100°C under nitrogen. A second breakthrough test was then performed at the same conditions of the first exposure with ammonia. Results of the second exposure would confirm irreversible ammonia effects.

PXRD

X-ray scattering patterns were obtained using a Bruker D8 Discover X-ray diffractometer in the locked-coupled (theta-theta) mode with monochromated Cu Kα (1.54 Å) radiation (40 kV, 40 mA) and scanned between 2θ = 1° and 50° with a step size (170.6 seconds/step) of 2θ = 0.021013°. Additional X-ray scattering patterns were obtained using a Siemens D5005 X-ray diffractometer in the locked-coupled (theta-theta) mode with Cu Kα (1.54 Å) radiation (40 kV, 40 mA) monochromated using a Gobel mirror and a thin film detector. Samples were mounted on a quartz low-background sample holder (limiting the characterization to shallow depth to avoid background signals) and scanned between 2θ = 5° and 120° with a step size (2 seconds/step) of 2θ = 0.02°.

$Cu_3(BTC)_2$ Reactions

$Cu_3(BTC)_2$–NH_4HCO_3 Reaction—18.3 mg $Cu_3(BTC)_2$ (30.2 μmol) was added to 1 mL D_2O containing 186 mg NH_4HCO_3 (2.4 mmole) with stirring. An immediate, clear, dark-blue solution formed. ^{1}H NMR spectra of the solution showed dissolved BTC (8.77 ppm) and DMF (8.29, 3.37 and 3.22 ppm), yielding an apparent mole ratio of 0.32 DMF per BTC. Thus, the $Cu_3(BTC)_2$ contained 7.5 wt% residual DMF.

BTC–NH_4HCO_3 Reaction—500 mg BTC (2.4 mmol) was dry-mixed with 600 mg NH_4HCO_3 (7.6 mmol) to which 0.5 mL H_2O was added with stirring. Immediate gas evolution indicated the desired reaction was occurring and it subsided after several minutes. The resulting material was allowed to dry in air to recover the solid $(NH_4)_3BTC$. ^{13}C CP-MAS NMR confirmed the identity and purity of the tri-substituted material.

BTC–$Cu(CO_3)Cu(OH)_2$–NH_4HCO_3 Reaction—100 mg BTC (480 μmol), 160 mg Cu $(CO_3)Cu(OH)_2$ (720 μmol), and 400 mg NH_4HCO_3 (5.1 mmol) were stirred in 1 mL H_2O. Immediate gas evolution resulted and the solution turned dark-blue. After stirring overnight the dark-blue solution was allowed to dry in air to yield a dark-blue solid.

NMR

^1H MAS NMR spectra were obtained using 30 to 45-degree pulses and relaxation delays of 1 to 2 sec on Varian Unityplus 300WB, INOVA 400WB and 600NB, and Bruker AVANCE 750WB NMR spectrometers equipped with Doty Scientific 7-mm Super Sonic (300WB and 400WB) and 5-mm XC (600NB and 750WB) VT-MAS NMR probes. ^{13}C MAS NMR spectra were obtained at 100.6 MHz on the Varian 400WB instrument and, for Cu_3BTC_2, direct excitation (90-degree pulses) and relaxation delays of 1 to 2 sec was employed (cross-polarization "CP" was not used). ^{13}C CP was used for the $(NH_4)_3BTC$ model compound (see below) using a 5 msec contact time and a relaxation delay of 2 sec. Solution NMR spectra were obtained on the Varian Unityplus 300WB NMR spectrometer using a standard 5-mm solution NMR probe. All spectra were referenced to external TMS.

Results and Discussion

Ammonia Breakthrough Capacity

Ammonia breakthrough experiments for once and twice exposed $Cu_3(BTC)_2$ samples were conducted. In the breakthrough curves, Figure 2–3, the twice exposed samples exhibit a significantly reduced ammonia capacity relative to the once exposed samples. Ammonia is known to be able to complex with either the copper atoms or the carboxylates of the MOF framework. The performance of the once and twice exposed $Cu_3(BTC)_2$ samples under both dry and humid conditions are summarized in Table 2. Integration of the breakthrough curve to saturation is used to calculate the dosage (concentration-time product, Ct) and capacity (retained ammonia mass per mass of $Cu_3(BTC)_2$). Note that substantial loss in capacity is exhibited by the twice exposed samples.

The shape of the first and second exposure breakthrough curves under dry conditions are similar, while those at humid conditions differ. The dry case indicates that thermal regeneration does result in partially restored adsorption capacity. The humid case first exposure suggests a slight discontinuity at approximately 50% of the feed concentration, perhaps a result of significant change in the structure of the $Cu_3(BTC)_2$. The humid second exposure sample shows rapid breakthrough consistent with loss of porosity.

The reaction under dry conditions indicates four mol NH_3 per mol $Cu_3(BTC)_2$ are sequestered. Thus, in the absence of water, the formation of a diammine-copper species is implicated which would allow up to six NH_3 if the reaction were to go to completion prior to ammonia breakthrough. Such a species, $Cu(NH_3)_2CO_3$, is known [25], and the compound undergoes slow decomposition upon exposure to moist air, apparently to $Cu(OH)_2Cu(CO_3)$. Scheme 2 shows the formation of the analogous compound for $Cu_3(BTC)_2$, "$Cu(NH_3)_2BTC_{2/3}$", under dry conditions, the carboxylates of BTC serving as the counter ion ligands rather than carbonate to form this indeterminate species. The moisture-promoted decomposition of the diammine

species is also shown, forming an indeterminate copper-hydroxide, the slight formation of which is detected by ^{1}H MAS NMR (see below).

With ample water, ammonium salts of the BTC might be anticipated to form (see Scheme 1) with concomitant formation of $Cu(OH)_2$. Thus, this first reaction, shown in Scheme 2, accounts for up to six NH_3. The capacity for NH_3 observed under humid conditions is consistent with Scheme 2, although it might be postulated that some NH_3 is solubilized by sorbed water or by the (limited) formation of tetraammine copper species which, as discussed in the Introduction, are known to form by the action of NH_3 on $Cu(OH)_2$ in aqueous solutions (Scheme 2). These proposed reactions for the dry and humid samples are consistent with ^{1}H MAS NMR characterizations (see below). In particular, ^{1}H MAS NMR (see below) detects a major species attributable to $Cu(OH)_2$ for the humid sample, but only slight formation of this species in the dry sample.

For the samples exposed a second time, the residual observed capacity for NH_3 can arise from 1) incomplete conversion during the first exposure (only 4.0 and 5.4 mole out of the possible 6 NH_3 per mol Cu_3BTC_2, respectively, are taken up by the dry and humid samples), 2) the formation of additional tetraammine copper (II) in the case of the humid material, and/or 3) some thermal decomposition of the di- and tetraamminecopper (II) complexes during activation to release their sequestered NH_3 as shown at the bottom of Scheme 2. Note that in the case of the dry sample "Cu_3BTC_2" *is not the original structure*, just the indeterminate material remaining following loss of the NH_3. For the dry sample, the presence of its greater residual capacity (1.7 mol NH_3 per mol Cu_3BTC_2) compared to that of the humid sample (0.6) could be simply due to residual, unreacted material (detected by XRD). The ammonium carboxylate species formed in the humid sample are apparently extremely stable salts which would not be expected to release NH_3 during activation to regenerate the free carboxylate; rather, as discussed above, ammonium is retained by carboxylates during heating, eventually forming amides when heated to sufficiently high temperatures (Scheme 1) – a reaction that would not regenerate NH_3 capacity.

The reactions depicted in Scheme 2 obviously involve the structural collapse of the metal-organic framework, creating materials of indeterminate structure. This is supported by PXRD data, as shown in Figure 5, and ^{1}H MAS NMR (see below). It should be noted that, in the presence of water, the reaction presented in Scheme 2 for the humid condition can indeed proceed to completion as confirmed by the observation that stirring a water-suspension of $Cu_3(BTC)_2$ with excess NH_4HCO_3 leads to its complete dissolution and an immediate deep-blue color, characteristic of the expected $[Cu(NH_3)_4(H_2O)_2]^{2+}$ complex (see Experimental).

Chiu[14] has determined the $Cu_3(BTC)_2$ cubic symmetry with the space group designation of Fm-3m. Using the deposited CIF file at the Cambridge Crystallographic Data Centre within the Cambridge Structural Database, one can use software such as Mercury to simulate the powder x-ray diffraction pattern. Comparing the simulated powder x-ray diffraction pattern with prepared $Cu_3(BTC)_2$ confirms the overall state of the starting materials prior to ammonia vapor exposure. In the case of $Cu_3(BTC)_2$ exposed to dry ammonia vapor, there is some clear indication that the $Cu_3(BTC)_2$ has lost some of its original crystallinity tending to a more amorphous material. The appearance of new peaks and disappearance of original peaks confirms the differences of crystal symmetry in the case of $Cu_3(BTC)_2$ exposed to humid ammonia vapor. Differences between different starting and humid ammonia vapor challenged $Cu_3(BTC)_2$ materials can be seen in the supplemental figures. A tabulation of the experimental and simulated PXRD peaks were compiled but no rigorous indexing has been carried out to fully characterize these differences. It was noted that there were some subtle differences between the experimental and simulation that are difficult to explain at present.

Nitrogen Adsorption Equilibria on Ammonia Exposed $Cu_3(BTC)_2$

Nitrogen adsorption isotherm measurements at the boiling point of nitrogen, 77.34 K, were performed on $Cu_3(BTC)_2$ before and after exposure to ammonia. Figures 6 shows a linear plot of the measured isotherm data and Figure 7 shows a log plot of the same data with amplification of the nitrogen adsorbed volumes at relative pressures below 10^{-1}.

In Figure 6, data show that the ammonia unexposed sample exhibits a classic Type I isotherm with a small amount of hysteresis. A majority of the nitrogen is adsorbed at relative pressures less than 10^{-3}. Molecular simulations of Ar adsorption isotherm data on similar Cu-BTC structures indicated that preferential adsorption exists in the tetrahedron side pockets of the lattice [15], indicating strong interaction energies within the microporous substrate, likely created by the unsaturated copper atoms.

The hysteresis loop at relative pressures above 0.4 corresponds to previous argon adsorption studies by Vishnayakov and coworkers, and is indicative of mesoporous defects formed during crystallization [15]. The exhausted samples exposed to ammonia under dry and 80% RH conditions show a significant decrease in nitrogen adsorption at all relative pressures. Under these conditions, the exhausted sample exposed to ammonia at 80 % RH has lost essentially all porosity. Figure 7 shows the same data as Figure 6 plotted on a logarithmic pressure scale. At low-to-mid relative pressures, the fresh $Cu_3(BTC)_2$ sample adsorb over 2 orders of magnitude more nitrogen than the exhausted samples. This is indicative of a loss of microporosity and is substantiated in the values calculated from the isotherm data.

Table 3 summarizes the BET capacity (or apparent surface area), the total pore volume, and the apparent micropore volume. The fresh material exhibits 10 times greater apparent surface area than the dry, ammonia once exposed sample and 100 times greater apparent surface area than the humid, ammonia once exposed sample. The apparent total pore volume is not greatly different between the three samples as this quantity is calculated at a high relative pressure, where all three samples show significant nitrogen adsorption. The apparent micropore volume indicate that the microporous channels of the fresh material have been greatly widened after exposure to both dry and humid ammonia challenges, further indicating that the porous network has rearranged.

Table 4 shows the measured capacities of the $Cu_3(BTC)_2$ for ammonia and nitrogen at a relative pressure equivalent to the ammonia feed concentration (1000 mg/m^3, Pi = 1.093 mm Hg, 298 K) used in the breakthrough experiments discussed above. The nitrogen capacity at 0.000145 relative pressure for the unexposed sample is higher than the ammonia capacity for the same sample by about 38%. Following exposure to ammonia, the nitrogen capacity decreases markedly to about 0.20 mL-N_2/g-sorbent, indicating complete collapse of the structure and loss of microporosity.

Based on the NH_3 capacity the N_2 isotherms are in good agreement for the capacity reduction associated with NH_3 adsorption and thermal regeneration.

NMR of Paramagnetic Compounds

For MAS NMR, $Cu_3(BTC)_2$ presents a challenge owing to its paramagnetic Cu(II). Ishii et al. [26] have pointed out the difficulty of assigning peaks as a result of large paramagnetic shifts and that line-narrowing by high-power proton decoupling is not as effective due to the large spectral distribution of paramagnetic shifts. Moreover, McDermott et al.[27] noted that wide spinning sideband patterns arise which are reflective of the large paramagnetic shift dispersion, chemical shift anisotropy, and bulk susceptibility anisotropy.

Yet McDermott et al.[27] point out that well-resolved MAS NMR spectra can be obtained in favorable cases where slow electron spin-lattice relaxation and electron spin-diffusion are effective at "decoupling" individual protons from the (normal) global proton dipolar-coupled spin system. In these instances carbon-proton pairs behave as isolated spin systems. Thus, when well-resolved ^{1}H MAS NMR spectra are observed, well-resolved ^{13}C MAS NMR spectra are also obtained without the need for high-power proton decoupling as reasonable MAS spinning rates are sufficient to overcome residual C–H couplings within spin pairs.

For example, Ishii et al. [26], in their ^{13}C MAS NMR study of Cu(alanine)$_2$(H_2O) (Figure 8), noted problems with decoupling the rigid methine and carboxyl groups with conventional cw ^{1}H decoupling at modest spinning speeds (ν_R = 5 kHz). However, they were still able to obtain good quality spectra using the ^{1}H self-decoupling provided by very fast MAS (ν_R = 24 kHz) of the "paramagnetically-isolated" putative CH and CH_3 spin pairs. Further, peak assignments were possible based on ^{13}C–^{1}H dephasing behavior, the effects of which were severe for CH (−269 ppm; rigid), moderate for CH_3 (173 ppm; rotating), and small for CO_2^- (−183 ppm; rigid, but no directly-attached protons). These assignments for Cu(alanine)$_2$(H_2O) are shown in Table 5. Thus, the observed strength of the ^{1}H–^{13}C dipole interaction, whether diminished by distance or internal motion, was still valid for making assignments in this paramagnetic complex. Such considerations regarding residual dipolar interactions can similarly be employed to render ^{13}C MAS NMR assignments for $Cu_3(BTC)_2$ and related model compounds (Figure 8) as discussed below.

^{1}H MAS NMR of $Cu_3(BTC)_2$

The most striking feature present in the ^{1}H MAS NMR spectrum of $Cu_3(BTC)_2$ (Figure 9) is the wide pattern of rather narrow spinning sidebands, indicative of a rigid-species unencumbered by homonuclear dipolar effects. The central peak of the sideband pattern is at 8.1 ppm and is straightforwardly assigned to the ring protons of the BTC constituent. There are at least two other similarly-sharp peaks which, lacking spinning sidebands, are obviously due to motionally-averaged species. Improvement in resolution was obtained at higher field, Figure 9, where near-baseline resolution is achieved for the three major peaks at 750 MHz (17.5 T) along with slightly-better resolution of smaller, overlapping peaks (see below).

The anhydrous form of $Cu_3(BTC)_2$ is purple whereas the hydrated form is blue[32]. Exposing a nominally-dry sample of $Cu_3(BTC)_2$ to air resulted in the series of spectra shown in Figure 10. It is clear from these spectra that adsorbed water yields the peak at ca. 12.6 ppm (H_2O ⋯ Cu), with all the peaks tending to shift upfield with increased water uptake. Further note that peaks assigned to residual, adsorbed *N*,*N*-dimethylformamide (DMF) (see below) are observed to be easily displaced/perturbed by water as previously noted by Chui et al. [14]. That adsorbed water shifts intensity from the downfield DMF peak to the upfield DMF peak is consistent with the assignment of these two peaks to DMF ⋯ Cu and DMF displaced to the channels, respectively (see below).

The identity of the remaining sharp ^{1}H MAS NMR peak(s) was inferred from ^{13}C MAS NMR spectra (see below) which revealed that the sample of $Cu_3(BTC)_2$ contained a considerable amount of DMF, apparently left over from its synthesis.[14] Heating a sample of $Cu_3(BTC)_2$ in air at 170 – 180 °C while intermittently observing the ^{1}H and ^{13}C MAS NMR spectra (Figure 11, left side) revealed immediate loss of the residual water peak at 12.7 ppm; slower loss of peak intensity at 7.1 ppm; and even slower loss of peak intensity at 9.7 ppm. Loss of intensity for the latter two peaks correlated with loss of intensity for DMF in ^{13}C MAS NMR spectra (not shown); thus, these two peaks are attributed to Cu(II)-bound DMF (9.7 ppm) and "channel-DMF"[14] (7.1 ppm) as a result of their relative desorption propensities. Also, these assignments are consistent with the water-displacement behavior noted above.

Further confirmation of the assignments of these peaks to adsorbed DMF was obtained by observing changes in ^{1}H and ^{13}C MAS NMR spectra after adding liquid DMF to the same sample (right side of Figure 11). In initial spectra, a broad feature at 2.3 ppm was observed to quickly dissipate within minutes whereas a second peak at −6.0 ppm persisted for days, and these peaks are attributed to bulk-DMF liquid and DMF sorbed on the (exterior) surface of the crystallites. The peaks of interest at 9.7 and 7.1 ppm remained unaltered while the sample sat at room temperature. Annealing the sample at 100°C for 23 h apparently assisted re-adsorption of DMF; first into the channels (7.1 ppm) and eventually coming to rest at the Cu(II) sites (9.7 ppm). Exposure to air restores the intensity of the water peak at 12.7 ppm with concomitant sharpening of the DMF peaks, presumably due to increased motion afforded by the co-adsorbed water. As further confirmation of these assignments, soxhlet-extracted (MeOH) $Cu_3(BTC)_2$ is totally devoid of both DMF peaks, leaving only the pristine methine spinning sideband pattern and a residual water peak (see Supplemental Material).

^{13}C MAS NMR of $Cu_3(BTC)_2$

^{13}C MAS NMR spectra obtained for $Cu_3(BTC)_2$, with and without high-power proton decoupling, are shown in Figure 12 (the large peak near 115 ppm common to both spectra is due to the Kel-F rotor endcaps). The difference between the two spectra is startling: In the absence of decoupling a sharp set of spinning sidebands is observed containing a center band at 228 ppm, whereas decoupling causes the sharp 228-ppm peak to vanish and the emergence of two broad peaks at 240 and 218 ppm along with their less-wide spinning sideband patterns. Such behavior is consistent with that observed by Ishii et al. [26] for Cu(alanine)$_2$(H_2O) (as discussed above) and for Cu(tartrate)(H_2O)$_3$ (see below). However, these changes are not observed for the sharp DMF peaks (165 and 38 ppm) and the wide spinning sideband pattern of broad peaks centered at −78 ppm.

It should be noted here that comparison of the intensity of the single, sharp DMF peak at 38 ppm to the sum of the peaks comprising the sharp spinning sideband pattern centered at 228 ppm reveals that the sample of $Cu_3(BTC)_2$ contains 0.47 DMF per BTC or about 10 wt % residual DMF. This value is comparable to that obtained from the complete dissolution of the $Cu_3(BTC)_2$ (see Experimental) which yielded 0.32 DMF per BTC or 7.5 wt % DMF.

With regard to the indifferent behavior of DMF to high-power proton decoupling, it is obviously undergoing rapid motion and, as a result, is “self-decoupled” from any static dipolar interaction. As for the static species at −78 ppm, it is apparently sufficiently-far and/or “paramagnetically-uncoupled” from the rigid-ring protons so that it experiences minimal ^{13}C-^{1}H dipolar coupling antics (see below). Assignment of this resonance to the BTC-CO_2^- group is consistent with its most-distal position relative to the ring-protons (and, hence, reduced static-dipolar interaction).

Considering the assignments of the remaining BTC-ring carbon peaks, they are not as straightforward as CO_2^- peak. Ishii et al. [26] employed ^{13}C–^{1}H dipolar recoupling to obtain unambiguous assignments of the paramagnetically-shifted peaks in Cu(alanine)$_2$(H_2O). This method was also applied to $Cu_3(BTC)_2$, where it was anticipated that ^{13}C–^{1}H “dephasing”[26] would be most pronounced for the protonated ring-carbon; less so for its non-protonated neighboring ring carbon; and least for the already-assigned CO_2^- group. These spectra, obtained with and without high-power proton decoupling, are shown in Figure 13. Solid $(NH_4)_3BTC$ was used as a diamagnetic control [26] for these experiments. The results show that the CO_2^- peak (−78 ppm) exhibits a dephasing ratio (S/S_o) [26] of 50 % which is close to the 44% value observed for this group in $(NH_4)_3BTC$, thus further affirming this assignment. However, the sharp peak at 228 ppm and broad peaks at 240 and 218 ppm exhibited quite similar ratios of 28 and 24%, respectively;* therefore, the assignments are still not entirely clear. By comparison, the non-protonated and protonated ring carbons of $(NH_4)_3BTC$ gave

very discriminating dephasing ratios of 38 and 12%, respectively. Yet a tentative assignment of the sharp 228 ppm peak to the (methine) protonated-ring carbon is suggested by its very similar appearance to the sharp peaks detected for the methine carbons in Cu(tartrate)$(H_2O)_3$ (see below). Furthermore, in ^{13}C CP-MAS NMR spectra recently obtained by Bertmer[xx] [[xx]Bertmer,M.; Poeppi, A.; Hartmann, M., "Multinuclear Solid-State NMR on Metal-Organic Framework Materials (MOFs)," poster presented at 50th Experimental NMR Conference, Pacific Grove, CA, Mar 29 – Apr 3, 2009] the sharp 228 ppm peak is the only carbon detected for $Cu_3(BTC)_2$—an observation entirely consistent with its assignment to the CH group. The remaining assignment of the non-protonated ring carbons falls to the broad peaks at 240 and 218 ppm. The presence of two peaks suggest inequivalent sites for this carbon; indeed, inspection of the crystal structure shows two sites adjacent to the channels whereas the third is distant, consistent with the approximate 2:1 ratio of the 240 and 218-ppm peaks. Finally, the fact that these peaks are not sufficiently decoupled by moderate-speed MAS alone may be due to the adjacent position of these carbons between two, otherwise paramagnetically-isolated C–H (methane) spin pairs. However, moderate-speed MAS is able to effectively narrow the more isolated (and separated) methine carbons.

The vanishing behavior of the sharp, MAS-decoupled peak at 228 ppm when high-power proton decoupling is applied is known to occur for ^{13}C–^{1}H dipolar interactions experiencing periodic effects such as molecular motion and/or spin-diffusion where maximum broadening is observed when the characteristic time of the decoupler field strength ($2\pi/\omega_1$) coincides with the correlation time (τ_c) of the modulation.[33] This behavior is indeed exhibited by the 228 ppm peak in spectra acquired under varied decoupling power (not shown). Thus, sufficient decoupler strength (ω_1) is not experimentally-possible to re-attain the line-narrowing condition $\omega_1\tau_c \gg 1$.[33]

MAS NMR of Cu(II) Model Compounds

The negative paramagnetic-shifting (−78 ppm) of the CO_2^- group adjacent to Cu(II) in $Cu_3(BTC)_2$ is in agreement with the negative shifts observed for groups adjacent to Cu(II) in Cu(alanine)$_2(H_2O)$: CO_2^-, −183 ppm, and CH, −269 ppm (Table 5).[26] Moreover, the positive paramagnetic-shifting of the peaks for the BTC-ring carbons more distant from the Cu(II) (240, 228, and 218 ppm) is consistent with the 173 ppm shift of the Cu(II)-removed CH_3 in Cu (alanine)$_2(H_2O)$. However, the other model compounds provide mixed results.

For example, consider the ^{13}C MAS NMR spectrum obtained for Cu(tartrate)$(H_2O)_3$, with and without high-power proton decoupling, shown in the bottom two spectra of Figure 14. ^{1}H MAS NMR spectra (not shown) yield two broad, equal-intensity, overlapping sideband patterns centered at about 6 and 4 ppm which, judging by the rather sharp ^{13}C MAS NMR spectra for the methine carbons (indicative of paramagnetically-isolated C–H spin systems, see above), are assignable to the two different methine protons[29], Figure 8. In the ^{13}C MAS NMR spectra, there are four different spinning side-band patterns, two of which are quite sharp (one in the presence of decoupling) and two of which are broad. The broadened side-band patterns are attributed to the two types of CO_2^- groups present in crystal structures of both the *meso* and *d*-tartrate Cu(II) compounds[29] (Figure 8), which are presumably also present in the Cu(*l*-tartrate)$(H_2O)_3$ model compound. The negatively-shifted set at −427 ppm is assigned to Cu–CO_2^-–H_2O by analogy to the negative-shift exhibited by the singly-Cu(II) coordinated CO_2^- group in Cu(alanine)$_2(H_2O)$[26] (−183 ppm, Table 5). The positively-shifted set at 483 ppm is then assigned to Cu–CO_2^-–Cu group. The shift assigned for the doubly-Cu(II) coordinated CO_2^- is quite close to the 501 ppm shift observed for the triply-bridging CO_3^{2-} group[31,34]

*Paramagnetic effects are assumed to be the cause of the virtually-identical dephasing ratios of the protonated and non-protonated ring carbons of Cu_3BTC_2.

in $Cu(CO_3)Cu(OH)_2$ (top spectrum, Figure 14). The remaining sharp resonances for the two types[29] of methines, which are quite identical in appearance to the sharp peak assigned to the methine in $Cu_3(BTC)_2$ (see above), are tentatively-assigned based on their proximity to the singly-Cu(II) coordinated and doubly-Cu(II) coordinated CO_2^- groups, with the positively-shifted methine (171 ppm) assumed to be adjacent to the positively-shifted CO_2^- (483 ppm) and the slightly-negatively shifted methine (−35 ppm) adjacent to the negatively-shifted CO_2^- (−427 ppm). Also, as discussed above for $Cu_3(BTC)_2$, the methine carbon at −35 ppm undergoes broadening under high-power proton decoupling whereas the methine at 171 ppm and both CO_2^- groups do not. This behavior is further evidence that the assignment of the −35 ppm methine is correct as this group is most-distant from the Cu(II) centers and would tend to experience reduced electron spin-diffusion "decoupling" effects.

Finally, Cu(II)-dimer compounds are of interest owing to their antiferromagnetic behavior, [35–37] i.e., they exhibit decreasing magnetic susceptibility with decreasing temperature leading to the complete disappearance of paramagnetism/magnetic susceptibility at sufficiently-low temperatures. Indeed, Oldfield et al.[28] only observed measurable ^{13}C MAS NMR signals for $Cu(formate)_2(C_5H_5N)$ at low temperatures, where the shift observed for the CO_2^- group at 163 ppm at 92 K is practically unshifted with respect to typical carboxylate groups in diamagnetic compounds (below 120 K only residual paramagnetism has been observed [37]). At higher temperatures, however, Oldfield et al. [28] observed broadening and upfield-shifting (negative) of the carboxylate peak until the signal was too broad to observe near 173 K owing to the onset of paramagnetic behavior.

Attempts at obtaining ^{13}C MAS NMR spectra of the cuprate-dimer $Cu(acetate)_2(H_2O)$,[38] which yielded a single, broad ^1H MAS NMR sideband pattern centered at 15 ppm, were unsuccessful, even at temperatures down to 173 K. The susceptibility of the acetate complex only becomes small below about 100 K [37] (attaining zero-susceptibility below 50 K[36]). Thus lower temperatures are required to observe ^{13}C MAS NMR spectra of Cu $(acetate)_2(H_2O)$ than our current instrumentation allows (133 K). With regard to $Cu_3(BTC)_2$, Williams et al. [39] have shown that its susceptibility is greatly reduced at room temperature relative to the formate and acetate compounds, which they surmise is due to weak ferromagnetic coupling between different Cu(II)-Cu(II) dimers as a result of the polymeric nature of this compound (in contrast to the discreet, molecular structures of other dimer compounds). Thus, it is evidently the polymeric nature of $Cu_3(BTC)_2$ which permits the observation of its ^{13}C MAS NMR spectrum at room temperature.

MAS NMR of $Cu_3(BTC)_2$ Interaction with NH_3

Kaskel et al. [32] previously noted that gaseous NH_3 adsorption causes irreversible changes to $Cu_3(BTC)_2$, but did not elaborate on the nature of the resulting material. Moreover, Yaghi et al. [11] concluded NH_3 had undergone chemisorption with $Cu_3(BTC)_2$ owing to its irreversible color-change from violet to light-blue. Thus, MAS NMR was employed to characterize the reaction between $Cu_3(BTC)_2$ and NH_3.

^1H MAS NMR spectra obtained following exposure of $Cu_3(BTC)_2$ to NH_3, under both dry and humid (80 % R.H.) conditions, are shown in Figure 15. The simple observation that, following both treatments, the simple, elegant, sharp spinning sideband pattern of the BTC-ring protons is drastically altered demonstrates that the basic structure has undergone dramatic change. Additionally, new features are consistent with the reactions presented above (Scheme 2).

For example, under dry conditions (Fig. 15a), the sharp Cu_3BTC_2 sideband pattern is replaced by two, broad spinning sideband patterns, one paramagnetically-shifted to −133 ppm and the other centered near the normal, (un-paramagnetically-shifted) range. Also evident are two sharp peaks lacking spinning sidebands at 3.1 ppm and ca. 0 ppm which are attributed to

residual DMF and a background impurity present in the empty rotor (presumably silicon grease), respectively. For the methine protons of BTC, disruption of the paramagnetically-induced “uncoupling” of the methine protons has occurred, restoring the normal, static dipolar interaction typical of a diamagnetic species; thus, the extremely-broad sideband pattern centered near 0 ppm is attributed to a BTC species which is less associated with the Cu(II) centers and experiencing its normal, strong dipolar ^{1}H-^{1}H coupling. Although diminished in breadth, the −133 ppm sideband pattern is quite similar to that of $Cu(CO_3)Cu(OH)_2$ (Fig. 15d) and is thus assigned to a $Cu(OH)_2$ species, the slight formation of which evidently occurred during handling of the sample in (moist) air. However, noticeably absent are signals for the anticipated (Scheme 2) diammine copper (II) complex. Saito and Kanda [40] observed ^{1}H NMR resonances for both NH_3 and H_2O in $Cu(NH_3)_4SO_4{\cdot}H_2O$ at liquid helium temperatures, but the prospect of obtaining spectra at higher temperatures was not discussed. An exhaustive literature search failed to find any other ^{1}H NMR studies of solid ammonia-copper (II) complexes. Therefore, it is likely that, owing to an unfavorable paramagnetic interaction with Cu(II), protons in the presumed ammonia-copper (II) complex present in the sample are not observable at room temperature (low temperature spectra were not investigated).

Under humid conditions (Fig. 15b) the −133 ppm sideband pattern for the $Cu(OH)_2$ species is more intense and its individual peaks are sharper; thus, NH_3 exposure, in the presence of water, is able to effect the expected conversion of Cu_3BTC_2 to $Cu(OH)_2$ (Scheme 2). The sideband pattern centered near 0 ppm is also sharper, perhaps owing to increased motion and/or solvation by water. Multiple peaks are also evident in the sideband patterns near zero which are assigned to the anticipated $(NH_4)_3BTC$ product (Scheme 2). Further, note that residual water and/or DMF peaks are broadened (compared to the corresponding signals in the dry-reacted material), apparently owing to contact with solvated Cu^{2+}. As discussed above for the case of the dry material, no peaks attributable to possible ammonia-copper (II) complexes are observed.

Finally, as shown in Figure 15c features of the two primary spinning sidebands observed in Figure 15b for NH_3-exposed Cu_3BTC_2 under humid conditions are faithfully reproduced by the reaction of BTC with $Cu(CO_3)Cu(OH)_2$ and NH_4HCO_3 in water (followed by drying), yielding an authentic mixture of the $Cu(OH)_2$ and $(NH_4)_3BTC$ products.

Conclusions

The metal-organic framework $Cu_3(BTC)_2$ reacts with ammonia to form a presumed diammine-copper (II) complex under dry conditions and, under humid conditions, a $Cu(OH)_2$ species and $(NH_4)_3BTC$; thus suffering an irreversible loss of structure and porosity. Initial removal capacities were on the order of 6 to 9 mol/kg at saturation, among the highest dynamic loadings for ammonia-removal sorbents; however breakthrough testing of exhausted samples reflects the significant decrease in available reactive sites and capacity. Nitrogen adsorption, PXRD, and NMR testing of fresh and exhausted samples all provide evidence for the permanent loss of structure and/or porosity, with samples challenged with ammonia under humid conditions undergoing the largest change. Although the porosity of the material is destroyed, the resulting capacity of the exhausted samples for ammonia is indicative of an extended reactive network consistent with that of the copper (II) complex products. Though antiferromagnet, ^{1}H and ^{13}C MAS NMR spectra of Cu_3BTC_2 are observable at room temperature and its paramagnetically-shifted resonances have been assigned. That the ^{13}C MAS NMR spectrum of Cu_3BTC_2 is observable at room temperature is consistent with its greatly-reduced susceptibility at room temperature compared to other Cu(II)-Cu(II) dimers.

Supplementary Material

Refer to Web version on PubMed Central for supplementary material.

Acknowledgments

The authors thank David Britt and Dr. Omar Yaghi of the University of California, Los Angeles, for synthesizing the $Cu_3(BTC)_2$ and providing PXRD data on fresh and exhausted materials and Dr. Marko Bertmer, Universitaet Leipzig, for helpful discussions regarding ^{13}C CP-MAS NMR studies of this compound. This work was completed under Joint Science and Technology Office for Chemical and Biological Defense (JSTO-CBD) Project No. BA07PRO104. Work performed on the high-field (17.5 T) NMR system at New York Structural Biology Center was supported under U.S. Department of Defense Contract W911NF0710053. NYSBC is a STAR center supported by the New York State Office of Science, Technology, and Academic Research. NMR Resources supported by NIH P41 GM66354.

References

1. Petit C, Karwacki C, Peterson G, Bandosz TJ. J. Phys. Chem. C 2007;111:12705–12714.
2. Petit C, Bandosz TJ. J. Phys. Chem. C 2007;111:16445–16452.
3. Yaghi OM, Li H, Davis C, Richardson D, Groy T. Acc. Chem. Res 1998;31:474–484.
4. Barton TJ, Bull LM, Klemperer WG, Loy DA, McEnaney B, Misono M, Monson PA, Pez G, Scherer GW, Vartuli JC, Yaghi OM. Chem. Mater 1999;11:2633–2656.
5. O'Keeffe M, Eddaoudi M, Li H, Reineke T, Yaghi OM. Journal of Solid State Chemistry 2000;152:3–20.
6. Braun ME, Steffek CD, Kim J, Rasmussen PG, Yaghi OM. Chem. Commun 2001:2532–2533.
7. Eddaoudi M, Li H, Yaghi OM. J. Am. Chem. Soc 2000;122:1391–1397.
8. Rowsell JLC, Millward AR, Park KS, Yaghi OM. J. Am. Chem. Soc 2004;126:5666–5667. [PubMed: 15125649]
9. Chen B, Ockwig NW, Millward AR, Contreras DS, Yaghi OM. Angew. Chem. Int. Ed 2005;2005:4745–4749.
10. Walton KS, Millward AR, Dubbeldam D, Frost H, Low JJ, Yaghi OM, Snurr RQ. J. Am. Chem. Soc 2008;130:406–407. [PubMed: 18154291]
11. Britt D, Tranchemontagne D, Yahgi O. Proc. Nat. Acad. Sci 2008;105:11623–11627. [PubMed: 18711128]
12. Dathe H, Peringer E, Roberts V, Jentys A, Lercher JA. Comptes Rendus Chimie 2005;8(3–4):753–763.
13. Dathe, Hendrik; Jentys, Andreas; Lercher, JohannesA. Physical Chemistry Chemical Physics 2005;7(6):1283–1292. [PubMed: 19791346]
14. Chui SSY, Lo SMF, Charmant JPH, Orpen AG, Williams ID. Science 1999;283:1148–1150. [PubMed: 10024237]
15. Vishnyakov A, Ravikovitch PI, Neimark AV, Bulow M, Wang QM. Nano Lett 2003;Vol. 3(No 6)
16. Vitillo JG, Regli L, Chavan S, Ricchiardi G, Spoto G, Dietzel PDC, Bordiga S, Zecchina A. J. Am. Chem. Soc 2008;130:8386–8396. [PubMed: 18533719]
17. Margerum DW, Rosen HM. Journal of the American Chemical Society 1967;89(5)
18. Martini G, Bassetti V. The Journal of Physical Chemistry 1979;Vol. 83(No 19)
19. Massey, AG. Comprehensive Inorganic Chemistry. 1st Ed.. Trotman-Dickenson, AF., editor. Oxford, UK: Pergamon Press, Ltd; 1973.
20. March, J. Advanced Organic Chemistry: Reactions, Mechanisms, and Structure. 2nd Ed.. New York, NY: McGraw-Hill; 1977.
21. Chen B, Eddaoudi M, Reineke TM, Kampf JW, O'Keeffe M, Yaghi OM. J. Am. Chem. Soc 2000;122:11559–11560.
22. Chen B, Ockwig NW, Millward AR, Contreras DS, Yaghi OM. Angew. Chem. Int. Ed 2005;44:4745–4749.
23. Yang Q, Zhong C. J. Phys. Chem. B 2006;Vol. 110(No 2):655–658. [PubMed: 16471581]
24. Rowsell JLC, Yaghi OM. J. Am. Chem. Soc 2006;128:1304–1315. [PubMed: 16433549]
25. Meyer MH, Singh P, Hatfield WE, Hodgson DJ. Acta Cryst.B 1972;28:1607–1613.
26. Ishii Y, Wickramasinghe NP, Chimon S. J. Am. Chem. Soc 2003;125:3438–3439. [PubMed: 12643699]

27. Liu K, Ryan D, Koji N, McDermott A. J. Am. Chem. Soc 1995;117:6897–6906.
28. Walter TH, Oldfield E. J. Chem. Soc., Chem. Commun 1987:646–647.
29. Prout CK, Carruthers JR, Rossotti FJC. J. Chem. Soc. A 1971:3336–3342.
30. Martin RL, Waterman H. J. Chem. Soc 1959:2960–2968.
31. Eby RK, Hawthorne FC. Acta Cryst. B 1993;49:28–56.
32. Schlichte K, Kratzke T, Kaskel S. Microporous and Mesoporous Materials 2004;73:81–88.
33. (a) Maricq MM, Waugh JS. J. Chem. Phys 1979;70:3300–3316. (b) Rothwell WP, Waugh JS. J. Chem. Phys 1981;74:2721–2732.
34. Zigan F, Joswig W, Schuster HD. Z. Kristallographie 1977;145:412–426.
35. Hay PJ, Thibeault JC, Hoffman R. J. Am. Chem. Soc 1975;97:4884–4899.
36. Figgis BN, Martin RL. J. Chem. Soc 1956:3837–3846.
37. Martin RL, Waterman H. J. Chem. Soc 1959:2960–2968.
38. Van Niekerk JN, Schoening FRL. Acta Cryst 1953;6:227–232.
39. Zhang XX, Chui SS-Y, Williams ID. J. Appl. Phys 2000;87:6007–6009.
40. Saito S, Kanda E. J. Phys. Soc. Jpn 1967;22:1241–1245.

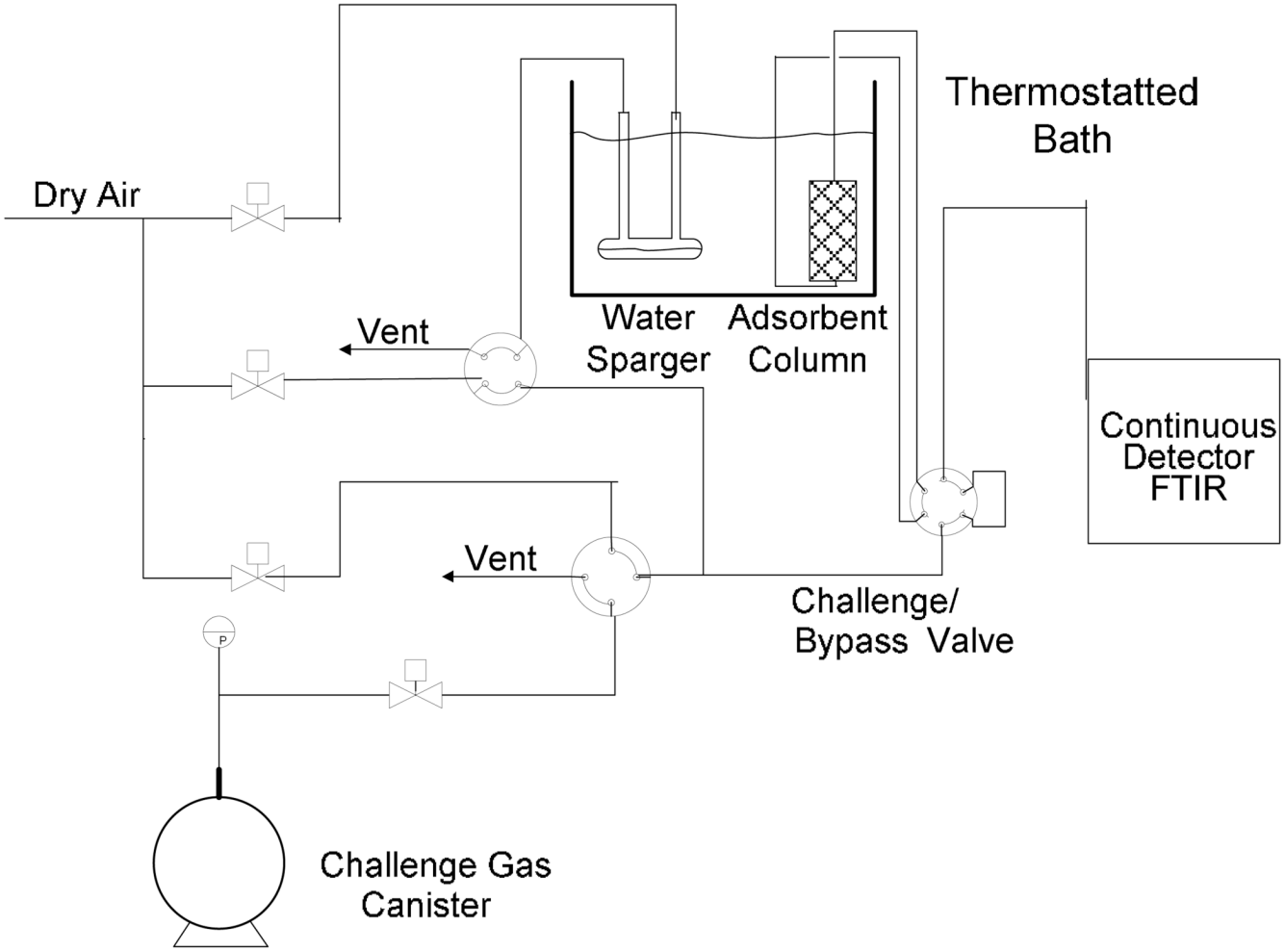

Figure 1.
Micro-breakthrough system schematic.

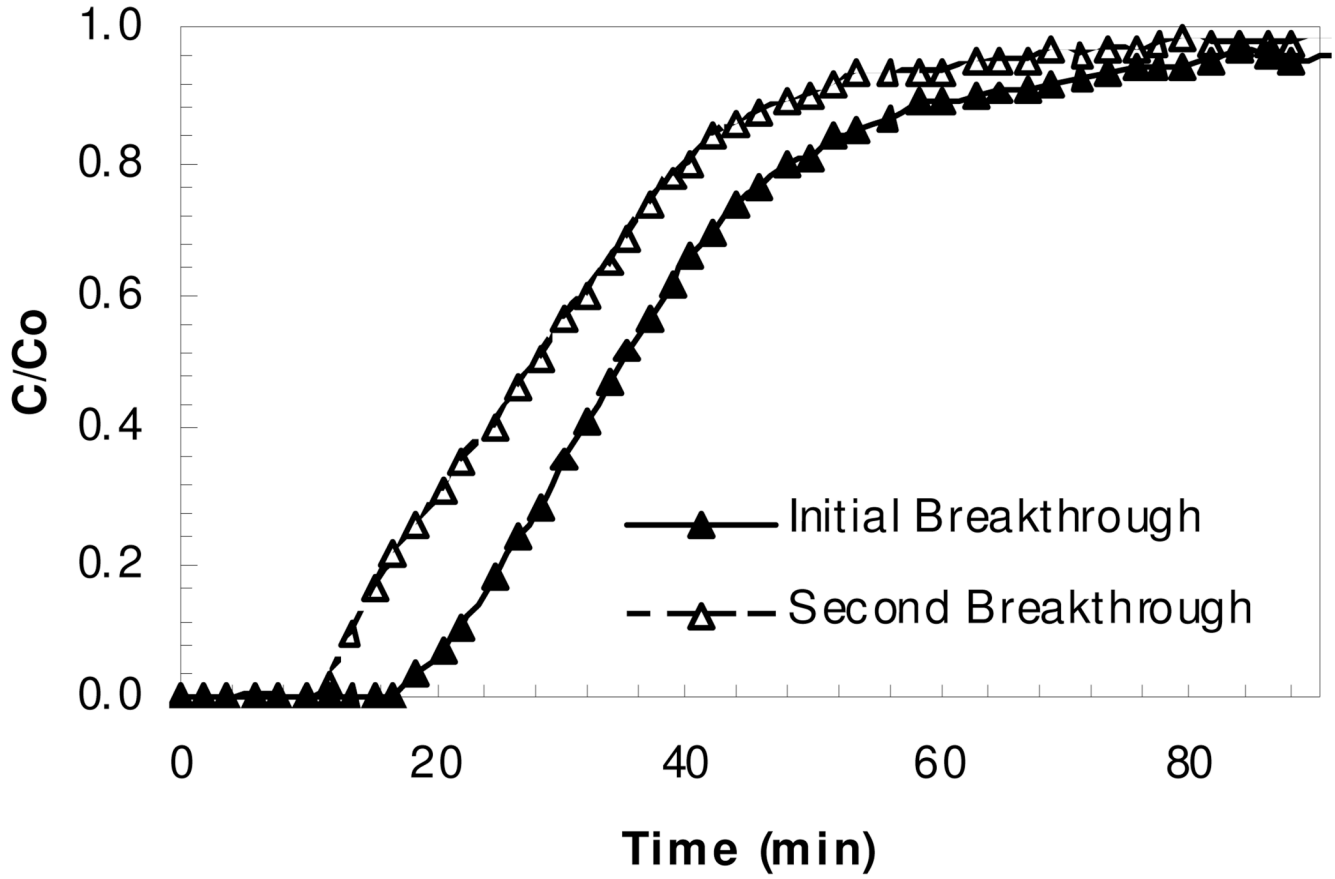

Figure 2.
Ammonia breakthrough of $Cu_3(BTC)_2$ in dry air.

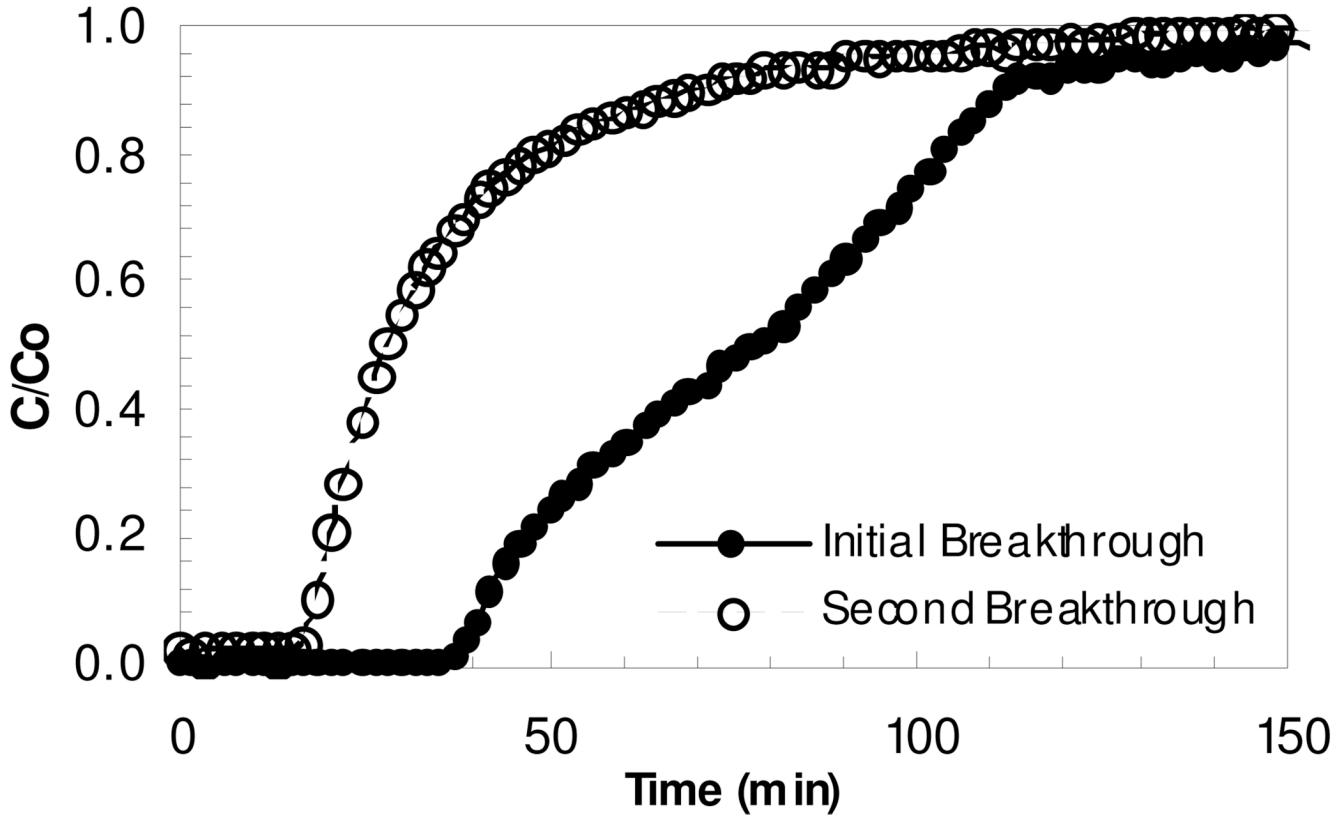

Figure 3.
Ammonia breakthrough of $Cu_3(BTC)_2$ at 80% relative humidity.

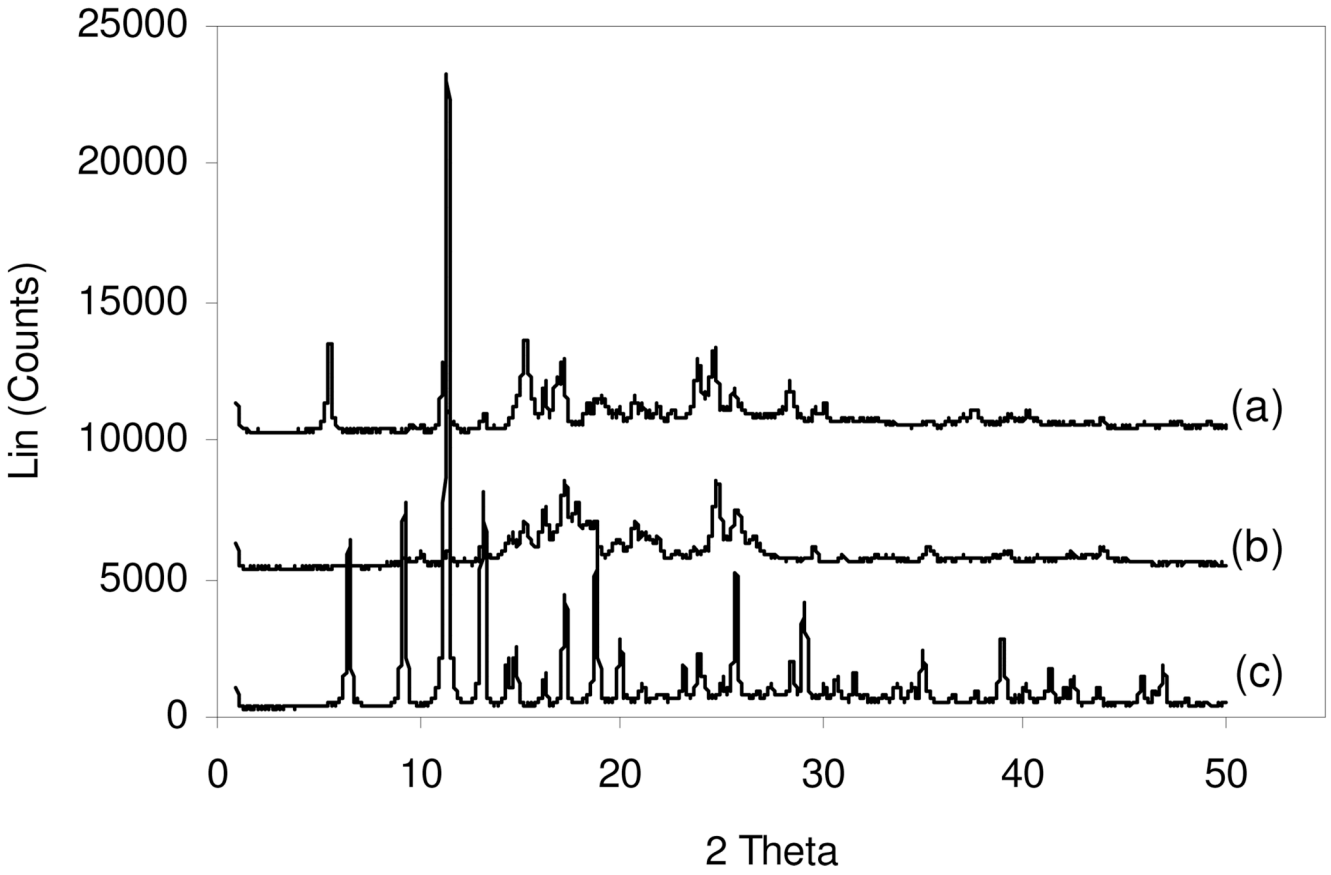

Figure 5.
PXRD data indicate that the humid once ammonia exposed (a) sample has a significantly different XRD pattern than the unexposed sample (c), indicating a complete change in the $Cu_3(BTC)_2$ framework. The dry once exposed (b) sample has a pattern somewhere in between the unexposed and once exposed humid samples.

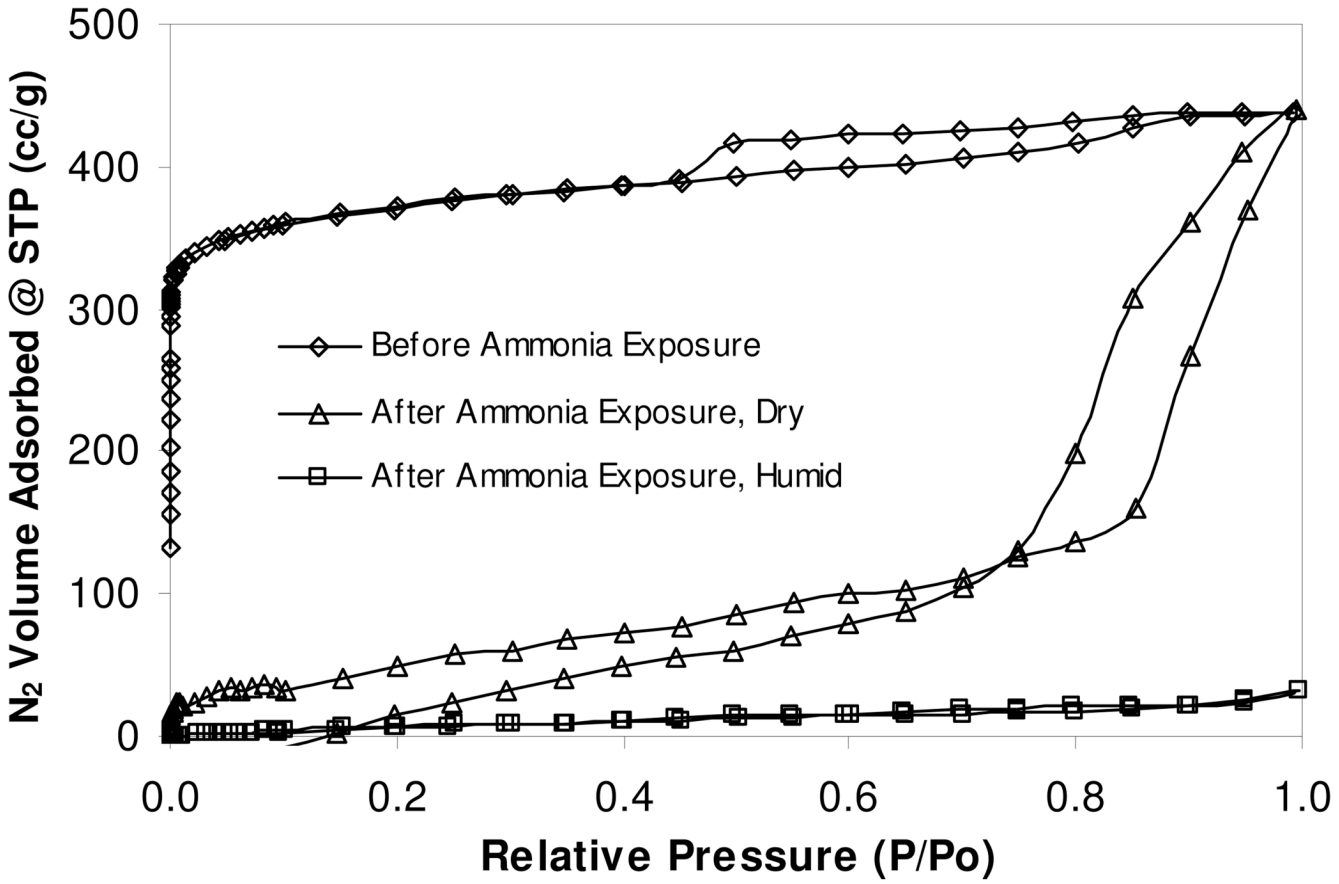

Figure 6.
Nitrogen isotherms of $Cu_3(BTC)_2$ before and after ammonia exposure. The dry, once exposed sample exhibits capillary filling, indicating the presence of some macroporosity, however the humid, once exposed sample has very limited nitrogen adsorption, indicating structural collapse and/or pore blockage.

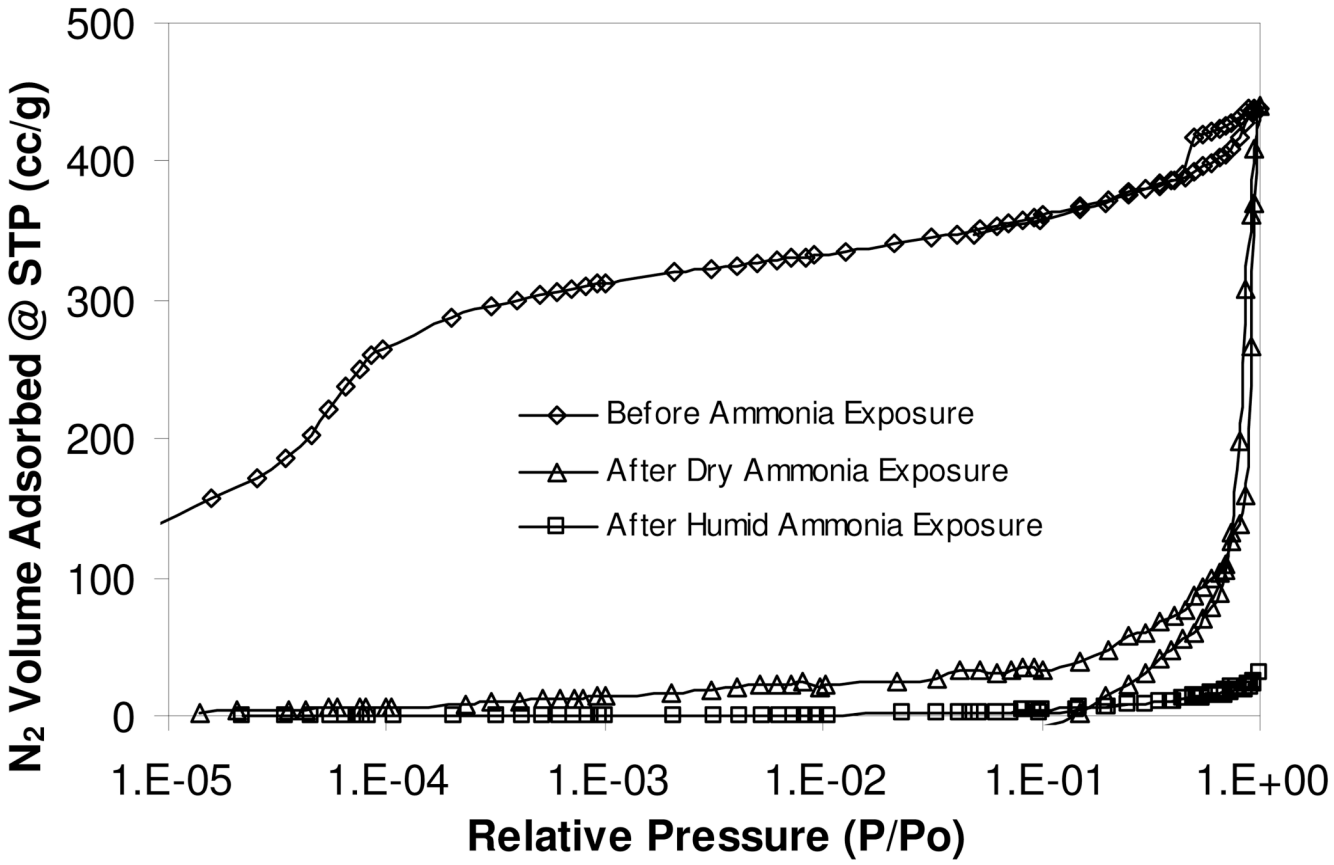

Figure 7.

Log plot of nitrogen isotherms of $Cu_3(BTC)_2$ before and after ammonia exposure. Neither the dry, once exposed nor humid, once exposed samples show any low-level nitrogen adsorption, indicating the absence of micropores.

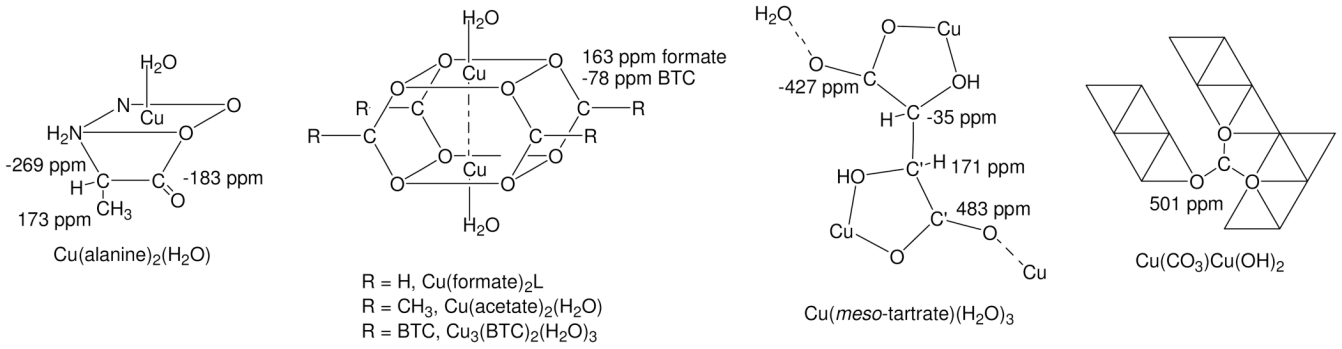

Figure 8.

Succinct structural elements of $Cu_3(BTC)_2$ and Cu(II)-containing model compounds indicating ^{13}C MAS NMR assignments. Assignments may be reversed for Cu(tartrate)$(H_2O)_3$ (see text). Although the structure for Cu(*meso*-tartrate)$(H_2O)_3$ is shown, Cu(*d*-tartrate)$(H_2O)_3$ (and presumably the *l*-tartrate model compound under study) similarly possesses the two types of CO_2^- and HCOH groups which are differentiated by prime notation[29]. The bi-nuclear Cu(formate)$_2$ core-structure shown is stabilized in the presence of amine-type ligands, but not water[30]. For $Cu(CO)_3Cu(OH)_2$ edge-sharing Cu(II) octahedral chains (two octahedrals wide) are represented by triangles, strips of which are linked[31] by the CO_3^{2-} group as indicated.

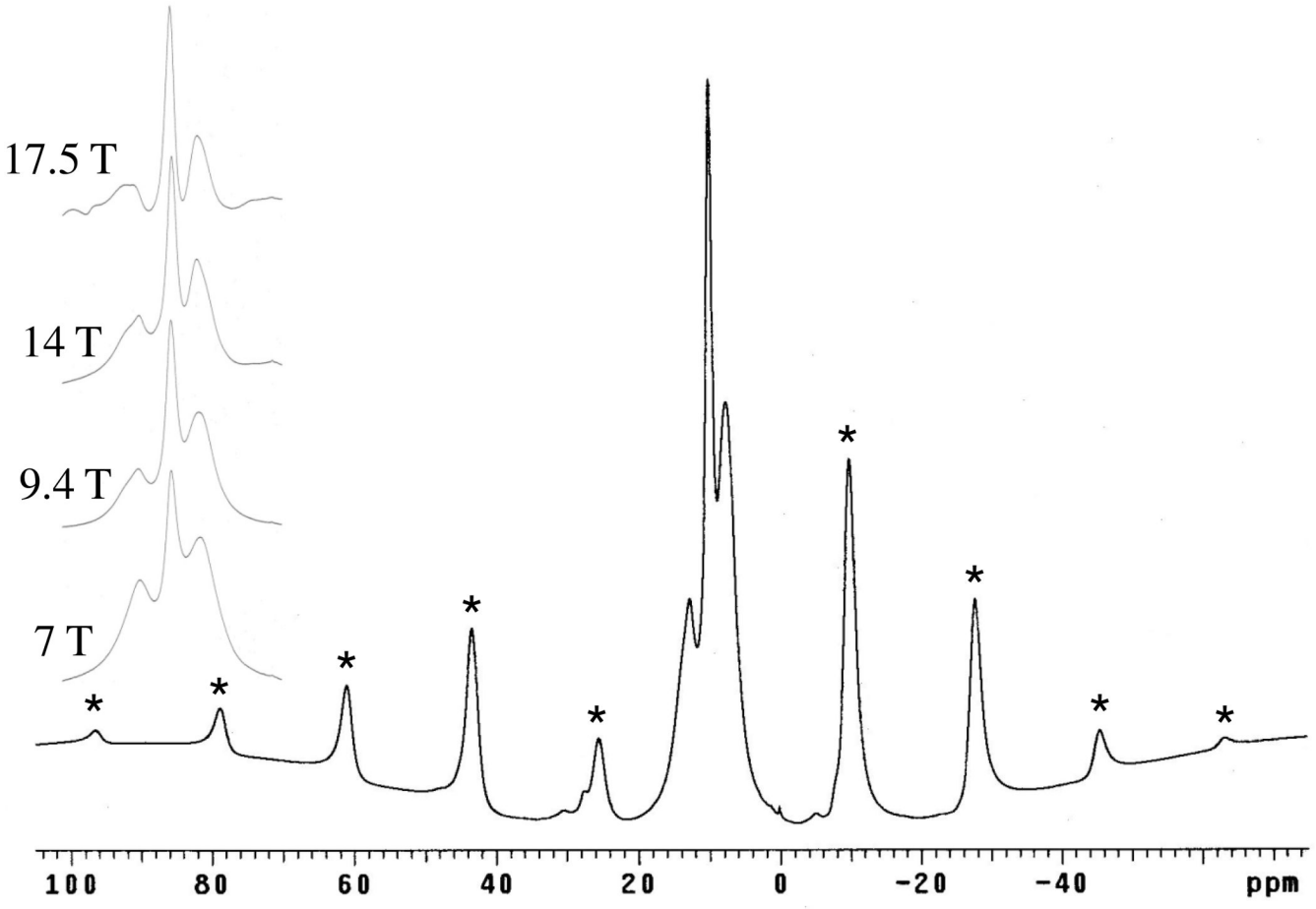

Figure 9.
400 MHz (9.4 T) ^{1}H MAS NMR spectra obtained for dry $Cu_3(BTC)_2$. Inset shows resolution of centerbands achieved at 7, 9.4, 14 and 17.5 T. Spinning sidebands are marked by asterisks.

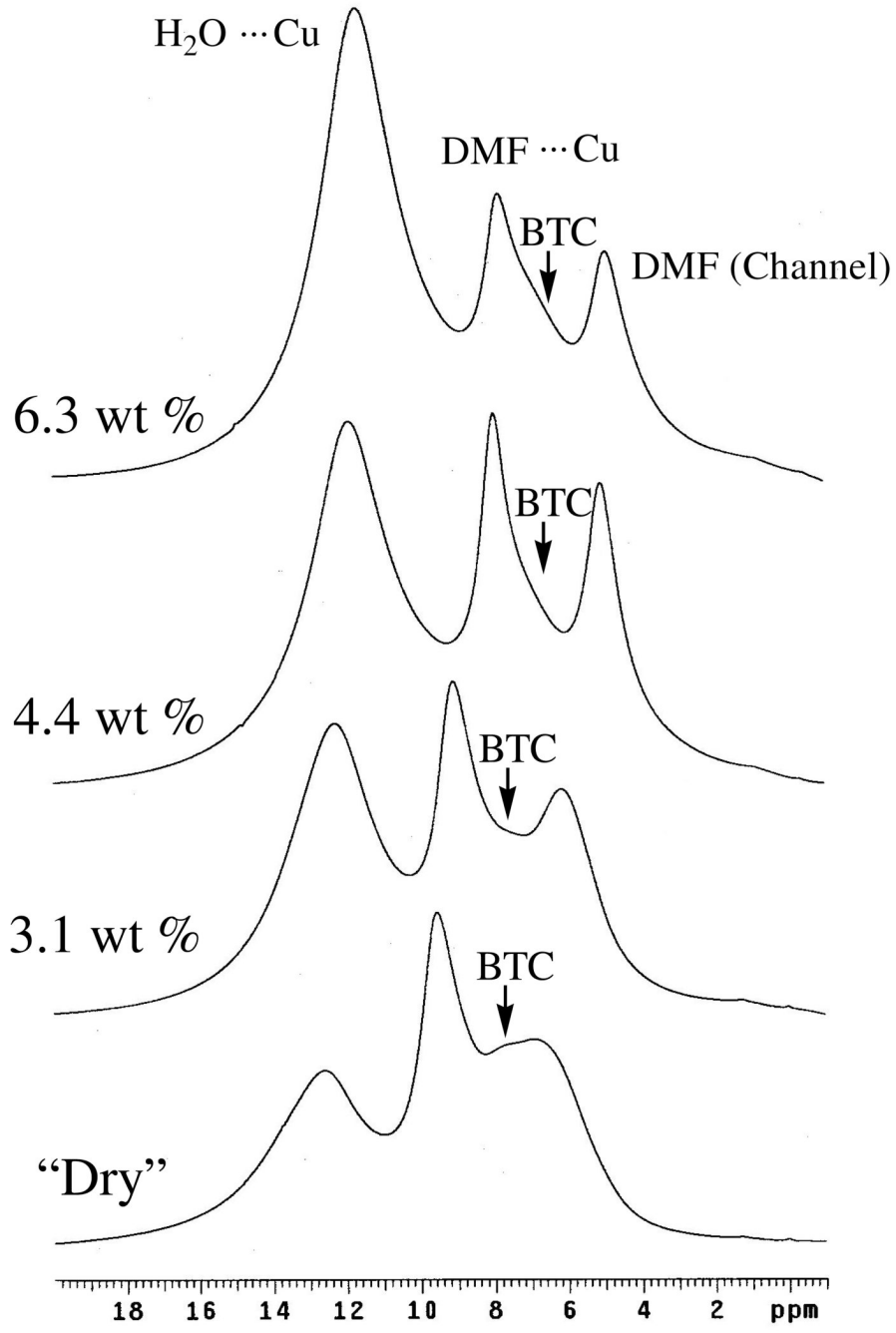

Figure 10.
^{1}H MAS NMR spectra (9.4 T) obtained for nominally-dry $Cu_3(BTC)_2$ before and after exposure to air for (bottom to top) 0, 2, 3.5, and 7 h. Percent weight gain is as indicated.

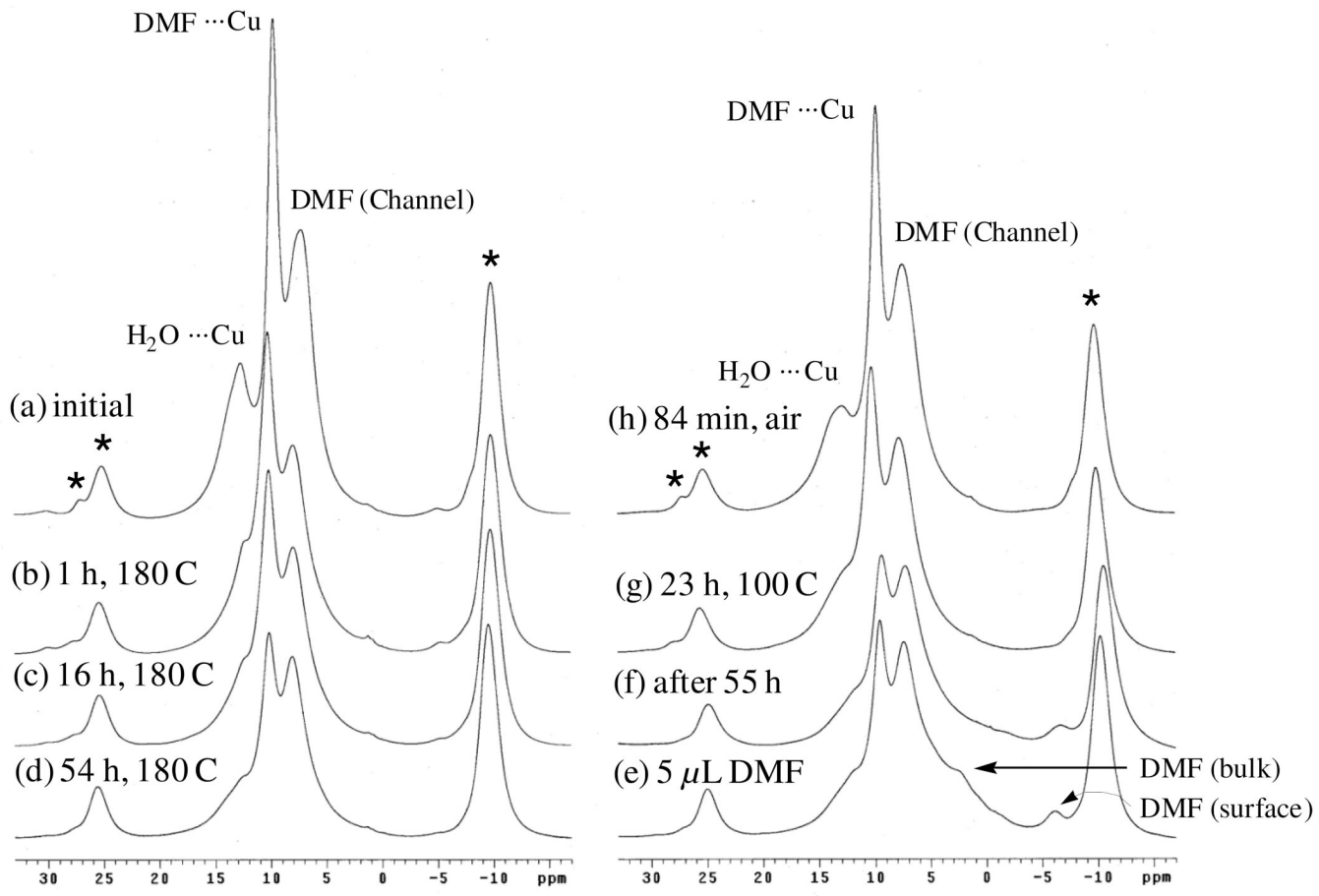

Figure 11.

^{1}H MAS NMR spectra (9.4 T) obtained for nominally-dry $Cu_3(BTC)_2$: (a) initial spectrum; (b) – (d) after heating to 180 °C to drive off water and DMF; (e) – (f) after addition of 5 μL DMF; (g) after heating to 100 °C to re-adsorb DMF; and (h) after exposure to air to re-adsorb water. Spinning sidebands are marked by asterisks at the top of each stack.

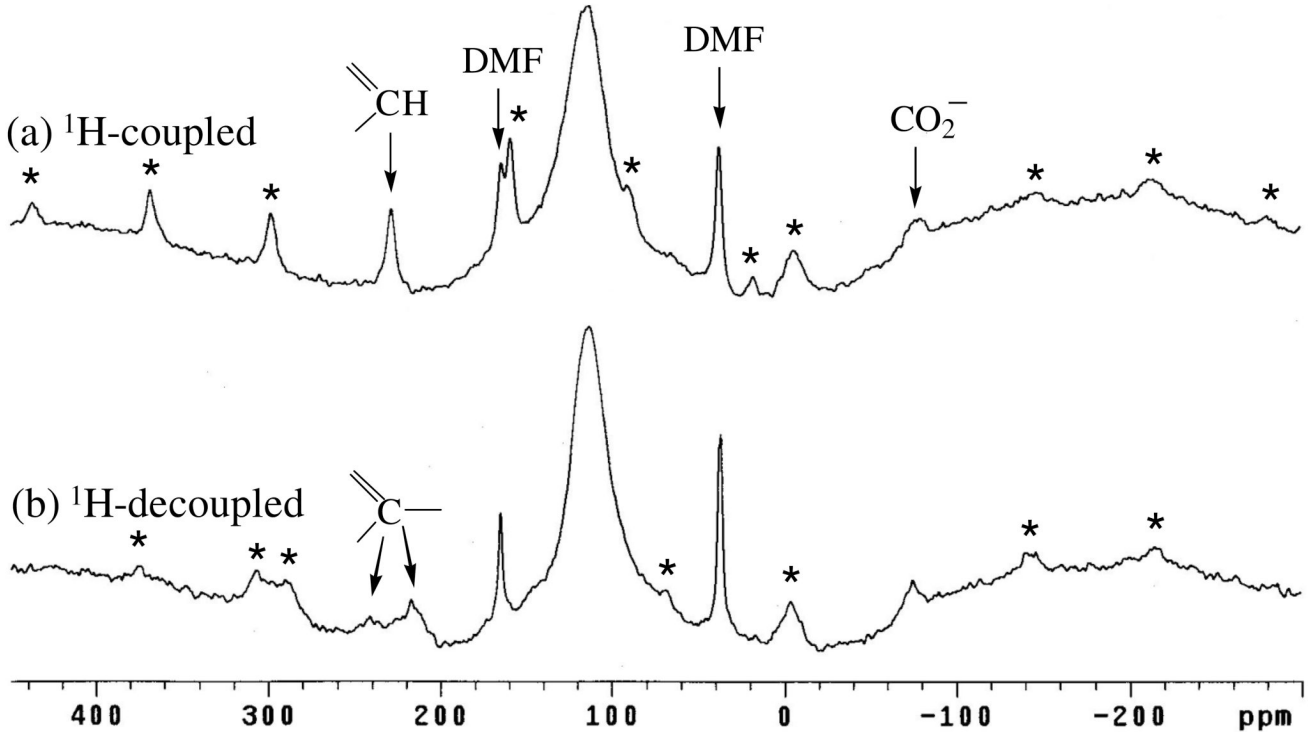

Figure 12.
^{13}C MAS NMR spectra (9.4 T) obtained for nominally-dry $Cu_3(BTC)_2$ without (a) and with (b) high-power proton decoupling. Assignments are indicated in the spectra (see text). Spinning sidebands (asterisks) and centerbands are indicated (see text).

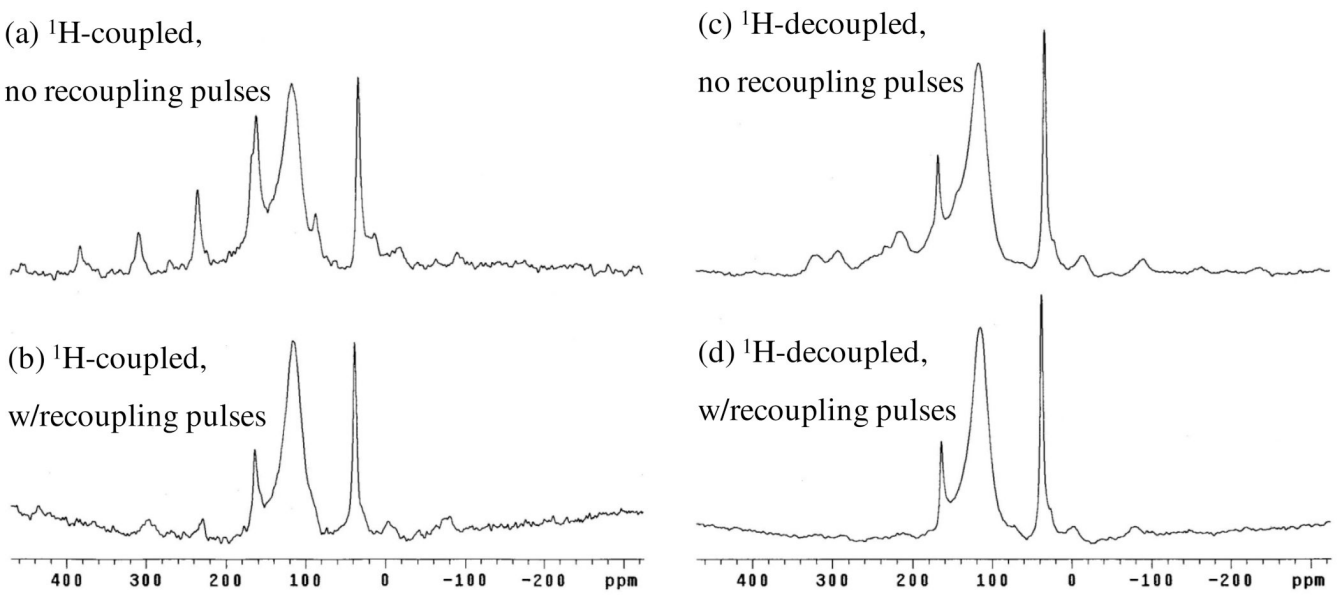

Figure 13.

^{13}C MAS NMR recoupling spectra (9.4 T, υ_R = 7000 Hz) obtained for nominally-dry $Cu_3(BTC)_2$ without (a,b) and with (c,d) high-power proton decoupling (see text).

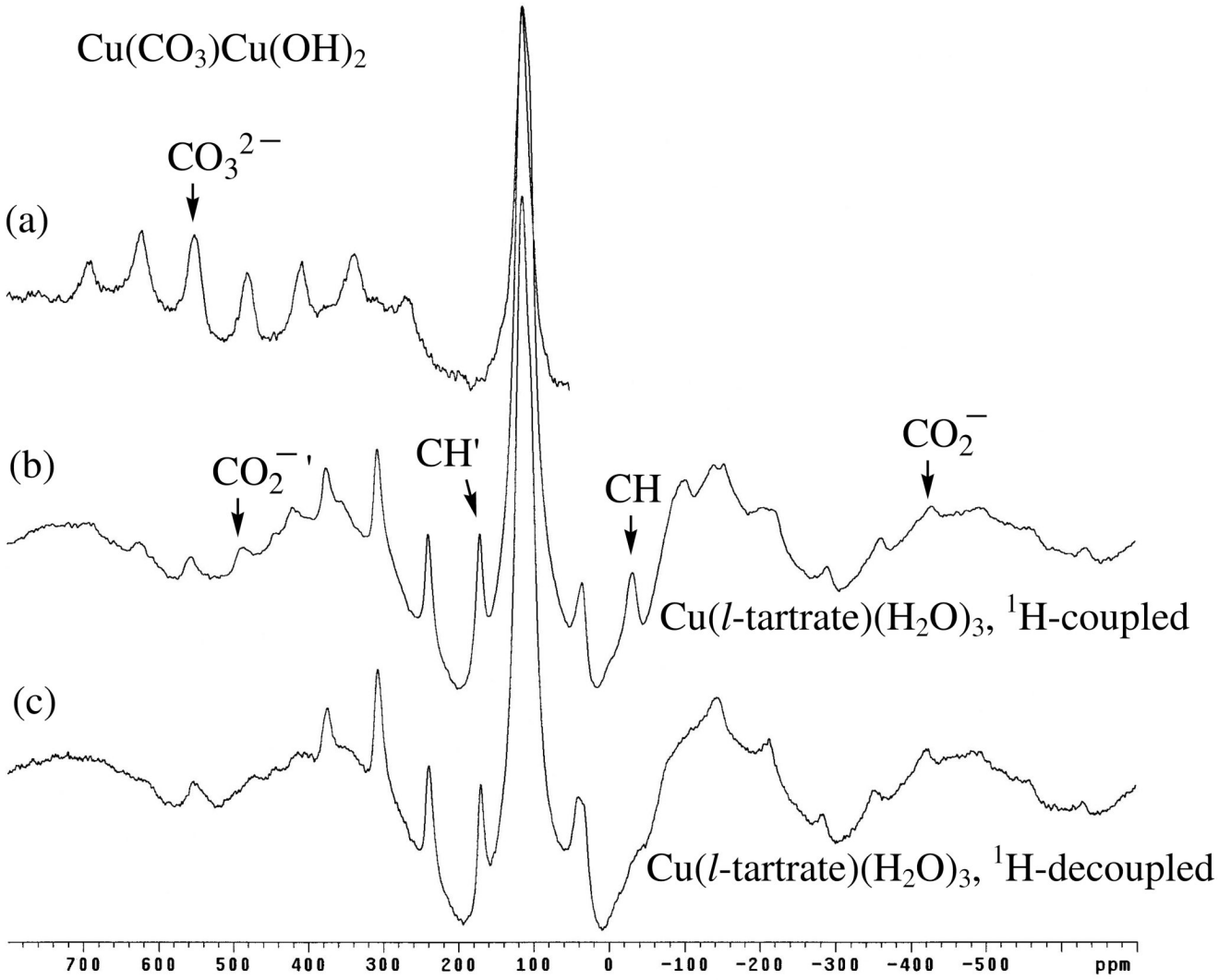

Figure 14.

^{13}C MAS NMR spectra (9.4 T) obtained for $Cu(CO_3)Cu(OH)_2$ (no decoupling), a) and Cu(*l*-tartrate)$(H_2O)_3$, without (b) and with (c) high-power proton decoupling. Centerbands of various spinning sideband patterns are indicated (see text).

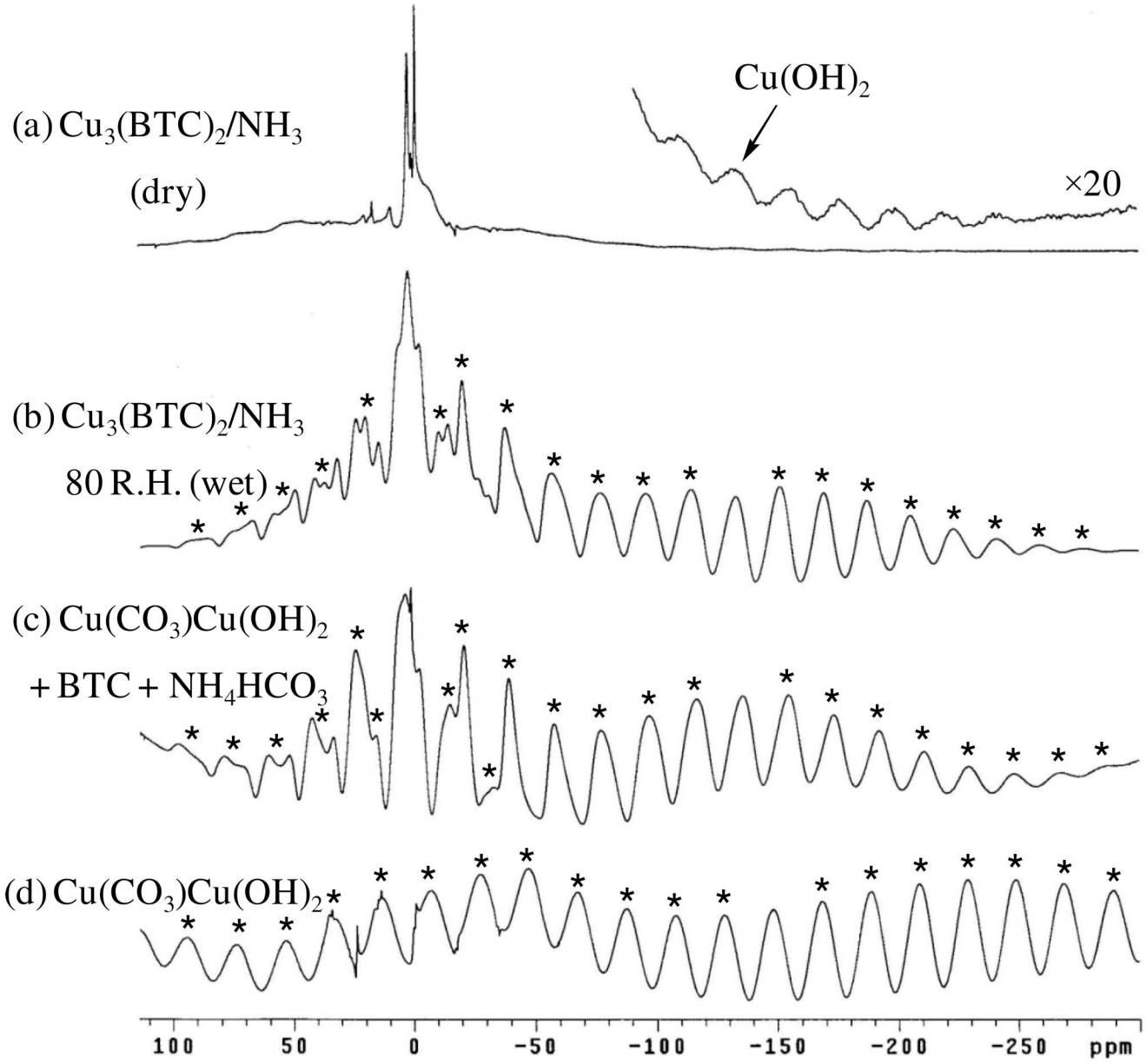

Figure 15.

^{1}H MAS NMR spectra obtained for $Cu_3(BTC)_2$ exposed to NH_3 under (a) dry (9.4 T, υ_R = 7000 Hz) and (b) humid (80 % R.H., 14 T, υ_R = 10,000 Hz) conditions. Spectrum (c) (9.4 T, υ_R = 7000 Hz) was obtained from the reaction of BTC with $Cu(CO_3)Cu(OH)_2$ and NH_4HCO_3 (see text). The spectrum of $Cu(CO_3)Cu(OH)_2$ ((9.4 T, υ_R = 7000 Hz) is shown in (d). Spinning sidebands are marked by asterisks in the lower spectra. Enhanced inset in spectrum (a) shows centerband for $Cu(OH)_2$ species (see text).

Scheme 1.
Generic amide formation.

Dry Condition:

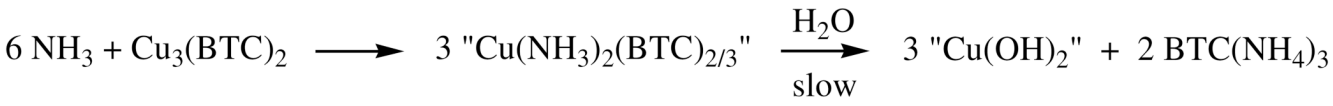

Humid Condition:

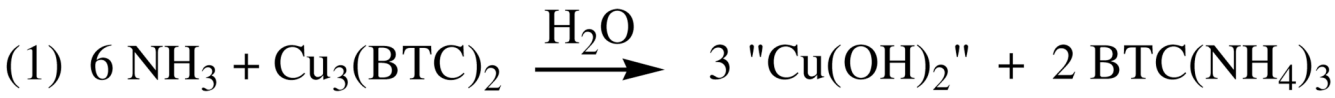

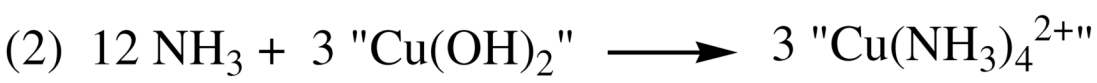

Activation of Spent Materials:

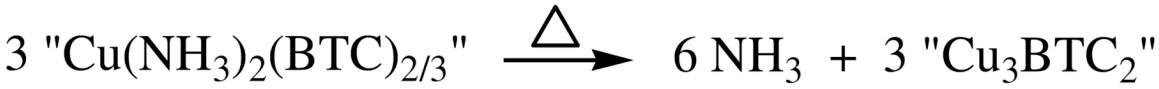

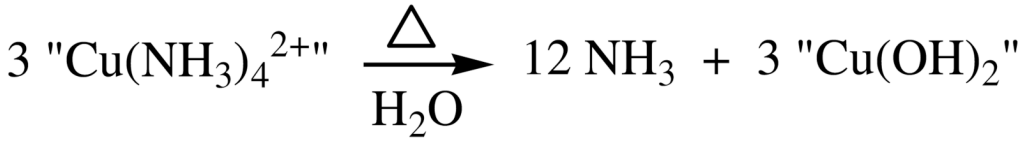

Scheme 2.

Table 1

Micro-Breakthrough Operating Conditions for Evaluation of $Cu_3(BTC)_2$.

Operating Condition	Value
Temperature	20 °C
Relative humidity	−40°C (~0%) dew point and 80%
Adsorbent mass	5–10 mg
Adsorbent volume	55 mm^3
Flow rate	20 mL/min
Airflow velocity	2.7 cm/s
Residence time	0.16 s

Table 2

NH_3 capacities of $Cu_3(BTC)_2$ samples

$Cu_3(BTC)_2$ Sample	**Capacity (mol/kg)**	**Capacity (mol/mol $Cu_3(BTC)_2$)**
Dry/First Exposure	6.6	4.0
Dry/Second Exposure	2.8	1.7
Humid/First Exposure	8.9	5.4
Humid/Second Exposure	1.0	0.6

Table 3

Calculated porosity and apparent surface area values from nitrogen adsorption isotherm data.

$Cu_3(BTC)_2$ Sample	BET Capacity (m^2/g)	Total Pore Volume at STP (cc/g)	DR* Micropore Volume at STP (cc/g)
Ammonia Unexposed	1,460	0.68	0.54
Dry once exposed	150	0.68	0.06
Humid once exposed	16.2	0.49	0.003

* Dubinin-Radushkevitch adsorption isotherm equation

Table 4

Ammonia and nitrogen adsorption capacity of $Cu_3(BTC)_2$

$Cu_3(BTC)_2$ Sample	Adsorbate	Relative Pressure	Capacity[1] (cc/g-adsorbent)
Dry Unexposed	Ammonia	0.000145	218.0[2]
Dry Unexposed	Nitrogen	0.000145	301[3]
Dry Once Exposed	Ammonia	0.000145	106.5
Dry Once Exposed	Nitrogen	0.000145	0.20

[1] Capacity at Pi/Ps = 0.000145, equivalent to 1000 mg/m^3 (1.093 mm Hg) NH_3, Psat = 7500.0 mm Hg at 298 K, V_m (NH_3) = 24.78 l/mol at 298 K.

[2] Ammonia capacity at 298 K determined from breakthrough measurements (see Table 2).

[3] Nitrogen volume adsorbed corrected to 298 K. See supplemental data S1.

Table 5

^{13}C and ^{1}H MAS NMR Shifts Observed for $Cu_3(BTC)_2$ and Model Compounds

Compound	Group	^{13}C(Temp)	^{1}H	Reference
$Cu(alanine)_2(H_2O)$	CO_2^-	−183 (331 K)	–	26 (^{13}C) 25 (^{1}H)
	CH	−269 (331 K)	8.4 (298 K)	
	CH_3	173 (331 K)	28.1 (298 K)	
	NH_2	–	−146 (298 K)	
$Cu(l\text{-tartrate})(H_2O)_3$	CO_2^-	483[a] (298 K)	–	This Work
	CH’	171[b] (298 K)	6 (298 K)[b]	
	CH	−35[b] (298 K)	4 (298 K) [b]	
	CO_2^-	−427[a] (298 K)	–	
$Cu(CO_3)Cu(OH)_2$	CO_3^{2-}	501 (298 K)	–	This Work
	OH^-	–	−148 (298 K)	
$Cu(formate)_2(C_5H_5N)$	HCO_2^-	163 (92 K)	–	28
$Cu(acetate)_2(H_2O)$	CO_2^-	No signals observed down to 173 K	–	This Work
	CH_3		15 (298 K)	
$Cu_3(BTC)_2 \cdot xDMF \cdot yH_2O$	CO_2^-	−78 (298 K)	–	This Work
	=CH−	228 (298 K)	8.1 (298 K)	
	=C<	240,218 (298 K)	–	
	H_2O	–	~12.7 (298 K)[c]	
	CH_3 (DMF)	38 (298 K)	9.7,7.1 (298 K)	
	HC=O (DMF)	165 (298 K)	ca. 12.7 (298 K)[d]	

[a] CO_2^- assignments may be reversed.

[b] CH assignments may be reversed.

[c] Peak shifts upfield with increasing water adsorption.

[d] Underlies H_2O peak.